remote sensing

MDPI

Article

Revealing the Land Subsidence Deceleration in Beijing (China) by Gaofen-3 Time Series Interferometry

Yakun Han [1,2], Tao Li [3,*], Keren Dai [1,4], Zhong Lu [5], Xinzhe Yuan [6], Xianlin Shi [1], Chen Liu [1], Ningling Wen [1] and Xi Zhang [1]

[1] College of Earth Science, Chengdu University of Technology, Chengdu 610059, China; yakunh@cdut.edu.cn (Y.H.); daikeren17@cdut.edu.cn (K.D.); shixianlin06@cdut.edu.cn (X.S.); liuchen2021@stu.cdut.edu.cn (C.L.); wenningling@stu.cdut.edu.cn (N.W.); qmqmqm3-zx@foxmail.com (X.Z.)
[2] Badong National Observation and Research Station of Geohazards, China University of Geosciences, Wuhan 430074, China
[3] Land Satellite Remote Sensing Application Center, Ministry of Natural Resources of China, Beijing 100048, China
[4] State Key Laboratory of Geological Disaster Prevention and Geological Environmental Protection, Chengdu University of Technology, Chengdu 610059, China
[5] Huffington Department of Earth Sciences, Southern Methodist University, Dallas, TX 75275, USA; zhonglu@smu.edu
[6] National Satellite Ocean Application Service, Beijing 100081, China; harley_yuan@mail.nsoas.org.cn
* Correspondence: lit@lasac.cn

Abstract: Revealing the land subsidence in Beijing, China, induced by the massive groundwater extraction in the past three decades, is important to mitigate the hazards and protect the residences and infrastructure. Many SAR (Synthetic Aperture Radar) datasets have been successfully applied to reveal the land subsidence over Beijing in previous research, while few works were achieved on land subsidence revealed by time-series InSAR (Interferometric Synthetic Aperture Radar) with Gaofen-3 SAR images. In this study, we successfully perform the time-series InSAR analysis with Gaofen-3 SAR images to extract the land subsidence in Beijing from 2020 to 2021. The Sentinel-1 SAR images were used to assess the accuracy of Gaofen-3 images. The subsidence scale and extent are consistent in detected major subsidence bowls between the two datasets. The spatial–temporal evolution and the deceleration of Beijing land subsidence were revealed by comparing with the Sentinel-1 results from 2017 to 2020. Moreover, we evaluated the interferometric performance of Gaofen-3 satellite SAR imagery and analyzed the main factors that mostly influence the coherence and quality of interferograms. Our results proved that the long perpendicular baselines decrease the coherence seriously over the study area, and the artifacts induced by inaccurate orbit information reduce the quality of the Gaofen-3 interferograms. Refining and removing the two main artifacts could improve the quality of interferograms formed by Gaofen-3 SAR images.

Keywords: interferometric performance; Gaofen-3; InSAR; subsidence; Beijing

Citation: Han, Y.; Li, T.; Dai, K.; Lu, Z.; Yuan, X.; Shi, X.; Liu, C.; Wen, N.; Zhang, X. Revealing the Land Subsidence Deceleration in Beijing (China) by Gaofen-3 Time Series Interferometry. *Remote Sens.* **2023**, *15*, 3665. https://doi.org/10.3390/rs15143665

Academic Editors: Joan Ramon Casas Rius, Jónatas Valença, Ling Chang, Xiaoqiong Qin, Jie Dong and Xuguo Shi

Received: 13 June 2023
Revised: 13 July 2023
Accepted: 16 July 2023
Published: 22 July 2023

1. Introduction

Land subsidence is a gradual geohazard that occurs in more than 150 countries; 19% of the global population may face a high probability of land subsidence by 2040 [1,2]. In China, more than 20 provinces are suffering serve land subsidence [3], including the land subsidence in Beijing Plain, where major subsidence bowls have been found in the district of Chaoyang, Changping, Haidian, and Tongzhou in recent decades. The region of land subsidence reached 770 km^2 during 2016–2018, which accounts for 12.05% of the total area of Beijing City; due to large–scale groundwater level depression, it has been the main threat to residences and infrastructure in Beijing. Monitoring land subsidence constitutes a critical and requisite component of land subsidence mitigation.

The spaceborne time series InSAR technique is an effective method to detect and quantify small displacements with wide coverage and high accuracy [4,5], which has been widely used in monitoring land subsidence [6–8], landslides [9,10], volcanoes [11], mines [12], and glaciers movements [13]. Several researchers have focused on the spatial–temporal dynamics of land subsidence over Beijing via InSAR based on varying time series methods and SAR datasets and have analyzed the causes of land subsidence by natural factors or anthropogenic activities (Table 1). However, few studies have been conducted for land subsidence based on Gaofen-3 SAR images using time series InSAR technology.

The Gaofen-3 satellite was launched on 9 August 2016. It is the first fully C–band polarimetric SAR satellite in China and is capable of acquiring high–resolution and large–width SAR images. It has been widely used in the application of ocean wind, ship detection, and terrain survey [14–17]. Wang et al., 2019 made an attempt to use only five Gaofen-3 SAR images to perform the land subsidence over Beijing using InSAR technology [18]—except that there is limited research and applications related to land subsidence monitoring based on Gaofen-3 SAR images via time series InSAR technology due to its imperfect interferometric performance. Therefore, it is essential to evaluate the interferometric performance evaluation of Gaofen-3 SAR images over Beijing.

Table 1. Summary of the relevant studies of land subsidence over Beijing using SAR satellites.

SAR Datasets	Time Range	Resolution	Maximum Subsidence Velocity	Studies
ERS-1/2	1992–2000	25 m	−48 mm/a	Zhang et al., 2016 [19]
Envisat	2003–2010	30 m	−143 mm/a	Chen et al., 2017; Guo et al., 2020; Zhu et al., 2020 [20–22]
ALOS-1	2007–2011	10 m	−120 mm/a	Du et al., 2021; Liang et al., 2013; Ng et al., 2012 [23–25]
Radarsat-2	2010–2016	30 m	−141 mm/a	Chen et al., 2020; Zhang et al., 2022; Zhou et al., 2019 [26–28]
TerraSAR-X	2010–2019	3 m	−117 mm/a	Bai et al., 2022; Chen et al., 2017; Zhou et al., 2022 [20,29,30]
ALOS-2	2014–2017	10 m/60 m	−150 mm/a	Du et al., 2018; Liu et al., 2021; Ning et al., 2019 [31–33]
Sentinel-1	2014–2020	20 m	−135 mm/a	Hu et al., 2019; Zhang et al., 2022; Zhu et al. 2020. [22,27,34]
Gaofen-3	2020–2021	3 m	**−80 mm/a**	**This study**

In this study, we evaluate the interferometric performance of Gaofen-3 SAR images to demonstrate its capability of interferometric and measurements, refine the quality of Gaofen-3 interferograms, and map the mitigation of land subsidence in Beijing in recent years based on Gaofen-3 SAR images. We apply the total coherence model to identify and discuss the major factors that impact the phase coherence and quality of Gaofen-3 interferograms and refine the artifacts in interferograms induced by inaccurate orbit information. We use time series InSAR (TS–InSAR) technology to generate high-accuracy subsidence maps based on the refinement interferograms of Gaofen-3 SAR images to reveal the mitigation of Beijing land subsidence in recent years.

2. Study Area and Datasets

2.1. Study Area

Beijing, as the capital city of China, is the national politics, culture, and technological innovation center of China and comprises 16 urban zones. It is located in the northern part of the North China Plain, 115.7°–117.4°E and 39.4°–41.6°N, covering an area of about 16,410.54 km^2. It is adjacent to the east of Tianjin city. The topography of Beijing is higher in the northwest and lower in the southeast, with an average altitude of about 43.5 m above sea level. It is surrounded by hills to the west, north, and northeast. The climate in Beijing is sub–humid and sub–arid monsoon with abundant rainfall in summer [35,36]. Due to the smaller swath of high–resolution Gaofen-3 SAR images compared to Sentinel-1 SAR images, we select the coverage of Gaofen-3 as our study area (indicated by the brown rectangle in Figure 1), which includes the districts of Changping, Shunyi, Chaoyang, Dongcheng, Xicheng, Haidian, and Shijingshan.

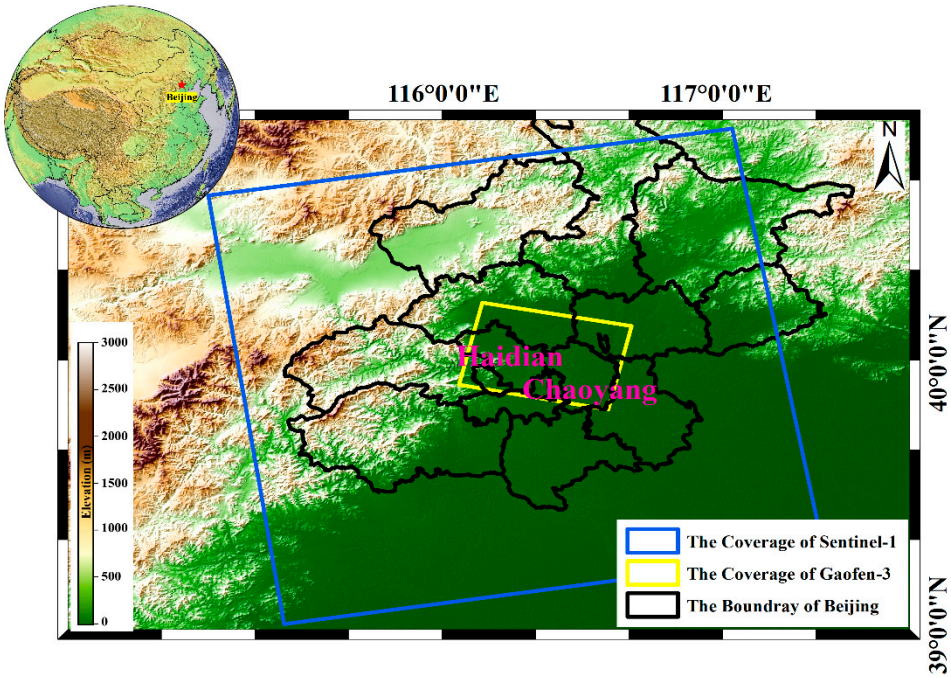

Figure 1. Location of the study area, the black lines delineate the boundary of Beijing City. The coverage of descending Gaofen-3 and ascending Sentinel-1 SAR images are marked by yellow and blue rectangles. The brown rectangle also indicates the study area.

2.2. Datasets

Since the Gaofen-3 satellite was not designed for InSAR applications, few SAR images could be used for time-series processing. The dataset includes 8 scenes of Gaofen-3 SAR images acquired from fine strip I (FSI) mode from June 2020 to March 2021 [15] and 111 scenes of Sentinel-1 SAR images acquired from strip mode (SM) from June 2017 to April 2021. In total, 17 scenes of Sentinel-1 SAR images from June 2020 to April 2021 were applied to assess the accuracy of Gaofen-3 SAR images, and 94 scenes of Sentinel-1 SAR images from January 2018 to August 2020 were used to reveal the subsidence trend over the study area. The coverage of the two datasets is shown in Figure 1. Both Gaofen-3 and Sentinel-1 operate C–band, with wavelengths of ~5.5 cm. The details of two SAR data are shown in Table 2. A 30 m Copernicus DEM was used to remove the topographic phase from the generated interferograms.

Table 2. Basic parameters of the SAR datasets over Beijing.

Sensor	Gaofen-3	Sentinel-1
Wavelength(cm)	5.55	5.54
Central frequency (GHz)	5.400	5.405
Incidence angle (°)	27.8145	39.1040
Resolution (Azimuth by range m)	1.12 × 2.61	2.32 × 13.93
Number of SAR images	8	111
Acquisition period	9 June 2020–26 March 2021	13 June 2017–4 May 2021
Band	C	C
Orbit direction	Descending	Ascending
Acquisition mode	FSI	SM

3. Methodology

To review the deceleration of land subsidence in Beijing. We first refined the quality of Gaofen-3 interferograms, and then we carried out the time-series InSAR method for descending Gaofen-3 datasets. Sentinel-1 datasets are applied to validate the accuracy of Gaofen-3 datasets in land subsidence measurements. Finally, combing the TS–InSAR

results of Sentinel-1 and Gaofen-3 datasets reveals the deceleration of land subsidence over Beijing. The overall workflow is shown in Figure 2.

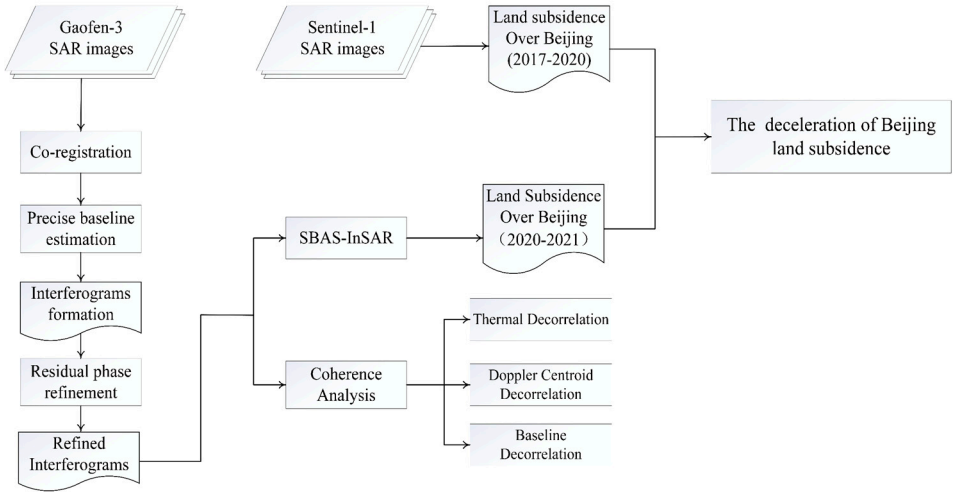

Figure 2. The flowchart reveals the deceleration of Beijing land subsidence by Gaofen-3 SAR images. It consists of the workflow of Gaofen-3 SAR images interferometry, interferometry analysis, time-series processing of Gaofen-3 SAR images, and the deceleration of Beijing land subsidence with Gaofen-3 results.

3.1. Index for Interferometric Performance Evaluation

The coherence of InSAR depicts changes in backscattering characteristics on the scale of the radar wavelength. It measures the quality of an interferogram, provides information about the types of the ground surface, and detects the small-scale changes in the scatter distribution. The coherence of InSAR is generally decreased by long baselines between satellites, long-time lags between image acquisitions, and random motions of scatters in resolution cells. Several sources of decorrelation could be expressed by correlation terms [37]:

$$\gamma = \gamma_{thermal} \cdot \gamma_{baseline} \cdot \gamma_{rotation} \cdot \gamma_{volume} \cdot \gamma_{temporal} \cdot \gamma_{other} \tag{1}$$

Thermal decorrelation, denoted by $\gamma_{thermal}$, is due to the thermal noise induced by the characteristics of the *SNR* of the radar system [38].

$$\gamma_{thermal} = \frac{1}{1 + SNR^{-1}} \tag{2}$$

$$SNR = 10lg(P_s / P_n) \tag{3}$$

P_s is the average received signal power, P_N is the power of thermal noise in the receiver system, and *SNR* is the signal-to-noise of the radar system.

Baseline decorrelation is a geometric decorrelation related to the baseline; the larger the perpendicular baseline, the greater differences between the primer and secondary SAR images. The baseline decorrelation could be simply defined as,

$$\gamma_{baseline} = \begin{cases} 1 - \frac{B_\perp}{B_c} & B_\perp < B_c \\ 0 & B_\perp > B_c \end{cases} \tag{4}$$

$$B_c = \frac{RB_w tan(\theta_{inc} - \alpha)}{f} \tag{5}$$

where B_c is the critical baseline of the InSAR system, it depends on radar frequency (f), bandwidth (B_w), and topographic slope (α).

The difference in Doppler centroid frequencies (Δf_{DC}) induced the geometric decorrelation in the azimuth direction, the coherence factor γ_{DC} decreases linearly with increasing differences in the Doppler centroid frequencies, as follows:

$$\gamma_{DC} = \begin{cases} 1 - \frac{\Delta f_{DC}}{B_A} & |\Delta f_{DC}| \leq B_A \\ 0 & |\Delta f_{DC}| > B_A \end{cases} \quad (6)$$

where B_A is the bandwidth in the azimuth direction [37].

3.2. SBAS-InSAR Method

Our approach for SAR data processing consists of the following steps: first, we generate a stack of Gaofen-3 and Sentinel-1 SAR images co-registered and resampled with respect to prior images using GAMMA software. After the fine registration and spectral offset filtering, we generated 28 Gaofen-3 interferograms based on the strategy of SBAS algorithms for taking full advantage of available SAR images. The temporal and perpendicular baseline thresholds of SBAS interferograms were 200 days and 2000 m, respectively. Then the flat-earth phase and topographic phase were removed in single-look interferograms. The combined orbit information and interferogram fringe frequency were applied to estimate the baseline [17,39]. The 2-D quadratic polynomial method was applied to model the residual phase of the baseline. Finally, the artifacts of residual orbit and atmospheric were removed from the wrapped interferograms based on the above method [40].

To maintain a high-quality correlation of interferograms, we applied a coherence threshold of 0.4 to select the interferograms for time series processing. We dropped some interferograms based on the mean coherence, the difference in Doppler centroid frequency, and some other artifacts from the refined wrapped interferograms. Only 9 of the 28 interferograms satisfied the criteria for SBAS-InSAR processing. Subsequently, we performed a time-series analysis using the SBAS-InSAR module in the software of StaMPS-InSAR (Standard Method for Persistent Scatters) [41,42].

The SBAS-InSAR technique employs all possible interferograms with small spatial and temporal baselines to improve the temporal sampling rate while maintaining high coherence. The SBAS algorithm in StaMPS was selected for time series processing, as this methodology could detect land subsidence by InSAR without prior information on land subsidence [43]. It could also identify the SDFP (slowly decorrelating filtered phase) pixels that surround by pixels that completely decorrelate on single-look images at the highest resolution [44]. The SDFP pixels candidates are initially selected by the amplitude difference dispersion index, as shown in Equation (6) [45,46],

$$D_{\Delta A} \equiv \frac{\sigma_{\Delta A}}{\mu_A} \quad (7)$$

Equation (7) is used to select the SDFP's candidates' pixels represented by $D_{\Delta A}$, where $D_{\Delta A}$ is the threshold value, $\sigma_{\Delta A}$ is the standard deviation of amplitude difference between the primer image and the second image, μ_A is the mean of a series of amplitudes values. The spectral filtering is then applied to multi-prime small baseline interferograms for SDFP pixel candidate selection. The decorrelation noise γ_x is estimated by subtracting the spatially correlated term and spatially uncorrelated term from the interferograms, calculating the variance of the residuals for the SDFP candidate pixels. The SDFP pixels are identified based on γ_x from amidst the pixels candidates.

$$\gamma_x = \frac{1}{N}\left|\sum_{i=1}^{N} exp\left\{\sqrt{-1}\left(\psi_{x,i} - \widetilde{\psi}_{x,i} - \Delta\hat{\phi}^{u}_{\theta,x,i}\right)\right\}\right| \quad (8)$$

where N is the number of interferograms, $\psi_{x,i}$ is the wrapped phase of pixel x in the ith interferogram, $\widetilde{\psi}_{x,i}$ and $\Delta\hat{\phi}^{u}_{\theta,x,i}$ are the estimated spatially correlated term and spatially

uncorrelated look angle error term [47,48]. Once the SDFP pixels are selected, the 3-D phase unwrapping method and deformation to phase solution are applied to the SDFP pixels [46,49,50].

4. Gaofen-3 Interferometry Analysis and Refinement

4.1. Gaofen-3 Interferometric Analysis

The InSAR coherence is a key factor in estimating the quality of interferograms which is related to the amount of phase error in interferograms. To understand the sources of decorrelation in the Gaofen-3 interferograms over Beijing, the interferograms from 27 January 2021 to 25 February 2021 of Gaofen-3 images (Figure 3a) were selected to analyze their interferometric performance. We also included the interferograms between 23 January 2021 to 28 February 2021 of Sentinel-1(Figure 3b) to assist in the analysis of Gaofen-3 SAR images (the details in Table 3). It can be seen from Figure 3 that the coherence performance and value of Sentinel-1 interferogram are better than those of Gaofen-3, especially in main urban distracts, and Figure 4 shows the histograms of coherence value for Gaofen-3 and Sentinel-1 interferograms represented by marigold color and green colors, respectively. The majority of coherence values for the Gaofen-3 interferogram fall within the range from 0.2 to 0.7, while the values of Sentinel-1 interferograms range from 0.3 to 0.9.

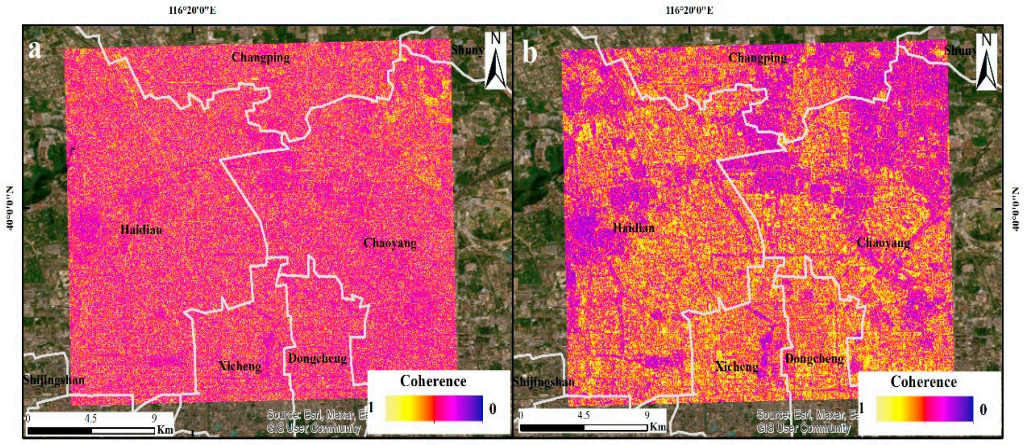

Figure 3. The coherence map of interferograms of the main urban districts of Beijing: (**a**) the coherence map of Gaofen-3 interferogram (27 January 2021–25 Febuary2021); (**b**) the coherence map of Sentinel-1 interferogram 23 January 2021–28 Feburay 2021).

Table 3. The characteristic parameters for phase decorrelation analysis.

Sensor	Gaofen-3	Sentinel-1
Date of interferogram	27 January 2021–25 Febuary 2021	23 January 2021–28 Febuary 2021
Coherence	0.4153	0.5138
NESZ (SNR^{-1})	−22.0 dB	−21.3 dB
Baseline of interferograms	1156 m	45 m
Critical baseline (B_c)	10 km	6.6 km

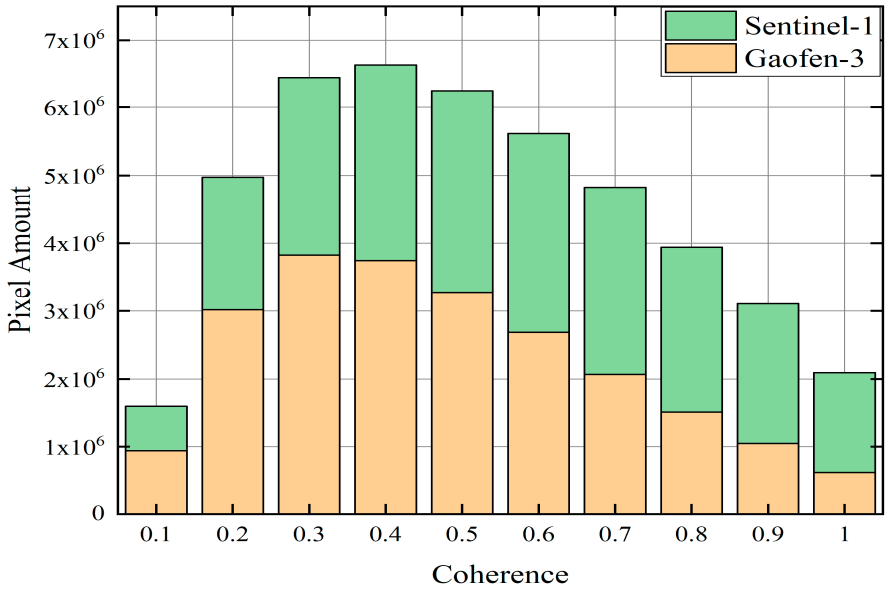

Figure 4. The statistics on pixel coherence for the Gaofen-3 SAR images (marigold color) and Sentinel-1 SAR images (green color).

A total coherence model is introduced to analyze the phase noise in the Gaofen-3 interferograms. According to the total coherence model (Equation (1)), the coherence of thermal noise was estimated by the value of the Signal Noise Ratio (SNR), where the Noise Estimation Sigma Zero (NESZ) as SNR^{-1} is used to estimate the coherence of thermal $\gamma_{thermal}$. The maximum NESZ is -21.3 dB and -22 dB for Gaofen-3 and Sentinel-1 satellites, respectively, so the SNR^{-1} is $10^{-21.3}$ and 10^{-22}, respectively [15,51]. The coherence of thermal $\gamma_{thermal}$ is close to 1 for both Gaofen-3 and Sentinel-1 based on Equation (2). Thus, the thermal noise is not the dominate inducement of the noise in Figure 3. Due to the similar time span of the two interferograms, the noise induced by temporal decorrelation $\gamma_{temporal}$ is also excluded. We also observed the difference in Doppler centroid frequency based on the parameters of the Gaofen-3 SAR data, where the difference in Doppler centroid frequency in this interferogram reached 19 Hz, and the azimuth bandwidth was 1482.5 Hz. Therefore, the decorrelation caused by the difference in the Doppler centroid is minimal and only takes up nearly 1% of the γ_{DC} decorrelation based on Equation (6).

The decorrelation of the baseline is the result of the difference in the incidence angle, the perpendicular, critical baseline (B_c), and the topographic slope of the earth's surface according to Equation (4) [37]. We derived the critical baseline (B_c) from the parameters of two satellites, which are approximately 10 km and 6.6 km for Gaofen-3 and Sentinel-1 based on Equation (5) (assuming there is no topographic slope). The larger the perpendicular baseline, the more serious the phase decorrelation to SAR interferograms over the study area.

Figure 5 shows that the perpendicular baselines of Gaofen-3 images range from 134 m to 1926 m, and most of them are more than 500 m, while the perpendicular baselines of Sentinel-1 images range between 2 m and 196 m. The maximum perpendicular baselines of Gaofen-3 are nearly ten times the perpendicular of the Sentinel-1 SAR data during the observation period. The perpendicular baseline is 1156 m for the interferogram of the Gaofen-3 images, which leads to the correlation of $\gamma_{baseline}$ decreasing to around 0.1156. While the perpendicular baseline is 45 m for the interferogram of the Sentinel-1 SAR images, the perpendicular baseline error to the coherence of the Sentinel-1 interferogram is negligible. Therefore, our results indicate that the Gaofen-3 SAR images own the capability of interferometric over Beijing city to a certain degree. However, the coherence is seriously contaminated by long perpendicular baselines, which limit the application of the Gaofen-3 images in ground surface monitoring.

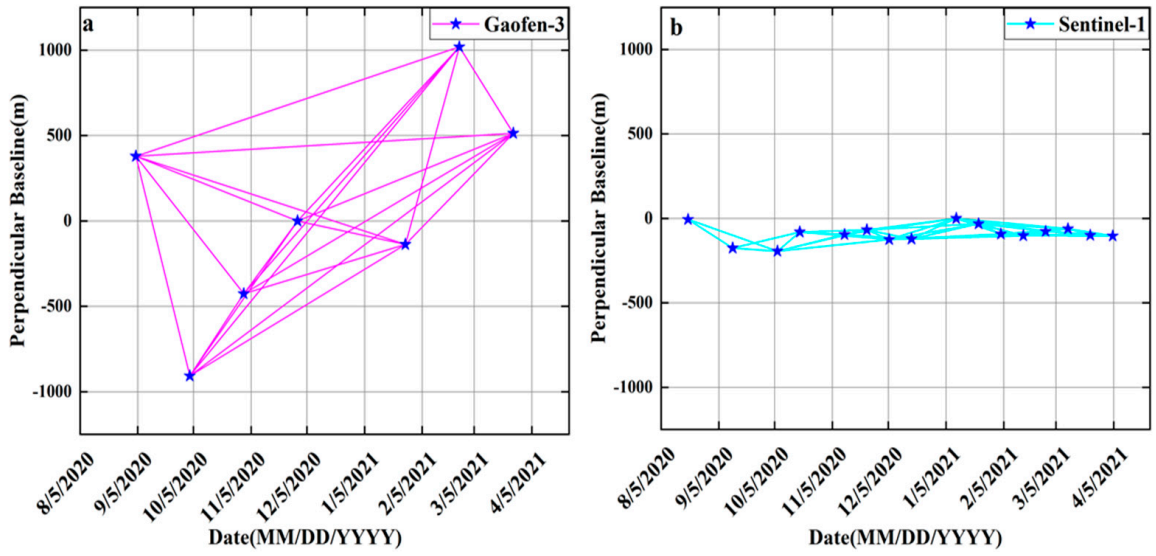

Figure 5. Spatial and temporal baseline distributions of the interferograms generated from the Gaofen-3 (**a**) and Sentinel-1 (**b**) SAR datasets from August 2020 to April 2021.

4.2. The Refinement of the Orbit-Related Artifacts

Figure 6 shows that when compared to the orbit track of the Sentinel-1 satellite, the orbit track of the Gaofen-3 satellite was unstable while observing the study area on different image acquisition dates. This instability led to a significant orbit error in range and azimuth direction. Due to the inaccurate orbit information of Gaofen-3, the accuracy of the perpendicular baselines calculated by orbital parameters could not reflect some changes in the azimuth.

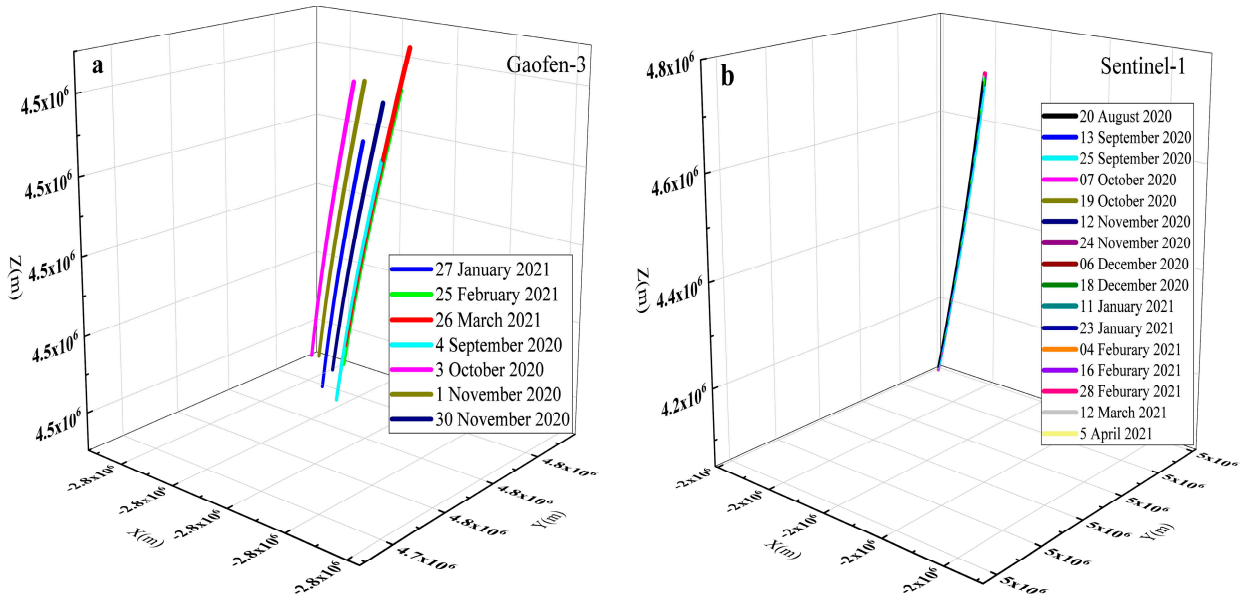

Figure 6. The track of SAR satellites based on the orbit state vector in image acquired date over the study area: (**a**) the track of the Gaofen-3 satellite observing the study area; (**b**) the track of the Sentinel-1 satellite observing the study area.

The spatial baseline errors usually increase the phase density and decreases the accuracy of phase unwrapping. The accuracy of baseline refinement will influence the quality of the interferograms. The conventional method uses orbit parameters to calculate the initial baseline, which assumes that the spatial baseline does not vary with time, which is suit-

able for parallel baseline estimation. Figure 7 shows that the high-density interferometric fringes in most of the wrapped interferograms resulting from initial baseline calculations are inaccurate by the errors in state vectors of orbit. In contrast, the interferogram itself could be used to improve the accuracy of perpendicular baseline estimation based on the interferogram fringe frequency. Therefore, we estimate the perpendicular baseline using the frequency information of the interferogram. Since the main frequency of the interferogram is not at the zero frequency, FFT (Fast Fourier Transformation) techniques were applied to shift it to zero frequency without assistance from the GCPs (Ground Control Points) and accuracy DEM.

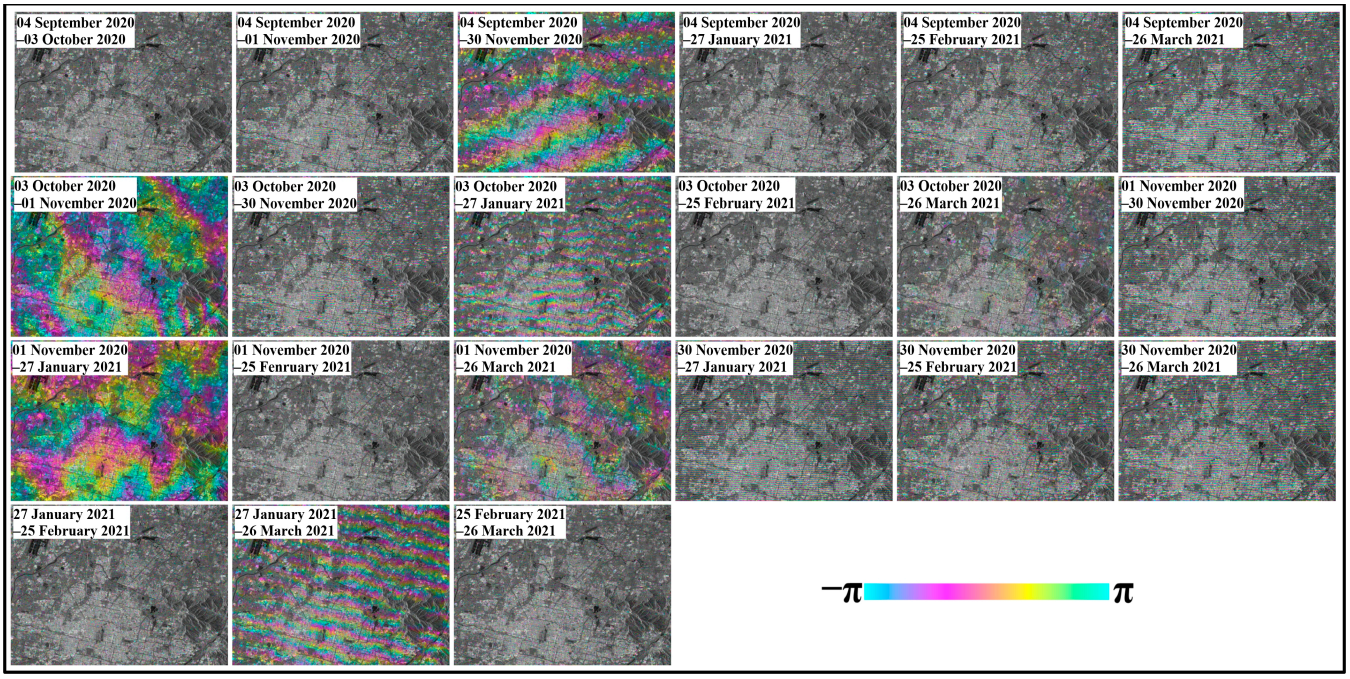

Figure 7. The wrapped interferograms with inaccurate orbit information of Gaofen-3 SAR images.

Due to the method of combined orbit information and interferogram fringes frequency without considering the detailed characteristics of the interferograms, the residual phase from the baseline errors still remained in wrapped interferograms. Furthermore, the baseline-induced error is often combined with atmospheric artifacts. Subsequently, the 2-D quadratic polynomial method is applied to model the residual phase of the baseline. After removing the phase-related interferometric baseline of the topographic, the height dependence of the atmospheric phase was modeled by a linear regression method. Then the residual orbit error and atmospheric are removed from the wrapped interferogram. As shown in Figure 8, the number of fringes was reduced greatly after removing the artifacts that related to inaccurate orbit information from the wrapped interferograms. However, the orbital phase is still obvious in some interferograms since we could not obtain the precise orbital information of the Gaofen-3 satellite during the observation period, and the orbital phase could not be estimated precisely.

There were no obvious baseline artifacts in the 10 interferograms that were processed using the StaMPS-InSAR technique. Therefore, the quality of the interferograms generated by the Gaofen-3 images is influenced by the artifacts with inaccurate orbit information. As for the artifacts related to the orbit in Gaofen-3, the interferograms serve more than those in other SAR satellites. Refining and removing the artifacts with inaccurate orbit information could assist the Gaofen-3 SAR images in achieving high-accuracy subsidence over the study area.

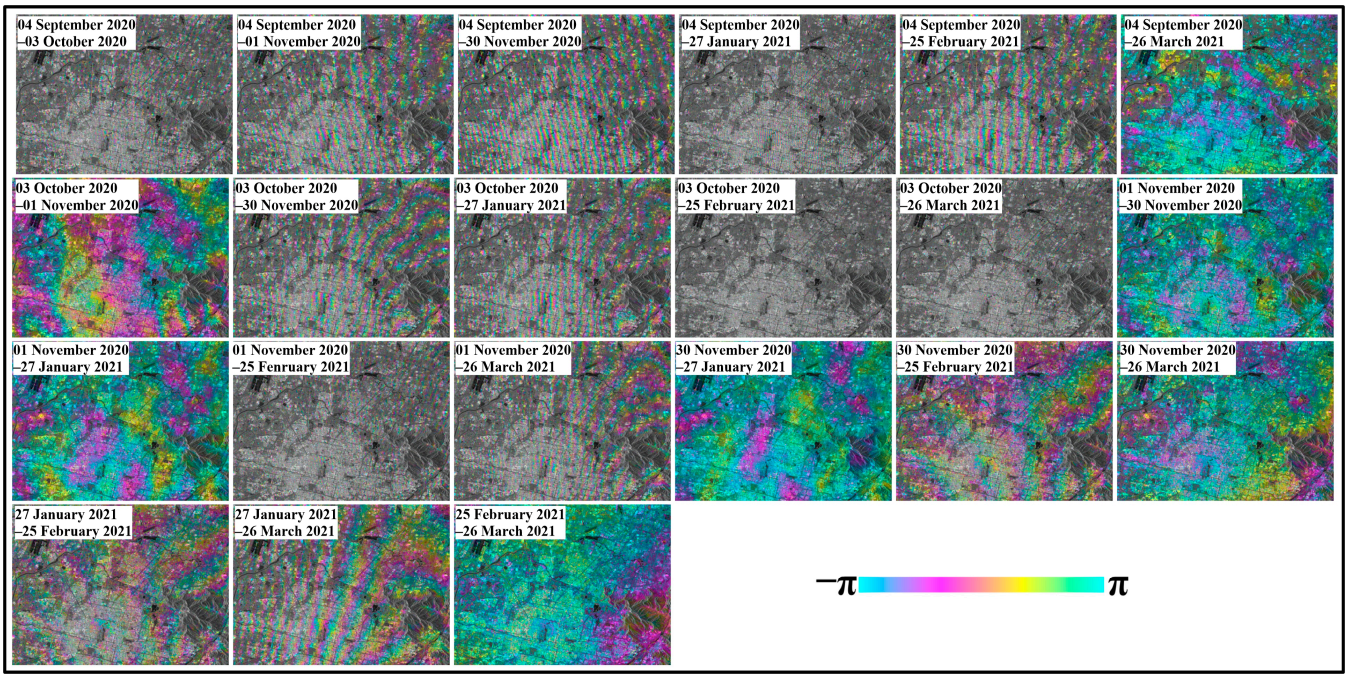

Figure 8. The refined wrapped interferograms of the Gaofen-3 SAR images by removing the orbit-related artifacts.

5. Gaofen-3 Time Series Results Analysis and Comparison

5.1. The Subsidence Results Acquired from Gaofen-3 Images

Since the incidence angles of the Gaofen-3 and Sentinel-1 SAR images are different, all the los (Line of Sight) velocities derived from the two datasets were converted into vertical direction by dividing the corresponding factor $cos\theta_{inc}$ (θ_{inc} is the incidence angle) to avoid incidence angle interference [25]. A map of mean velocity derived from the Gaofen-3 SAR images over the study area from September 2020 to April 2021 is shown in Figure 9. The negative velocities represent the subsidence (red color) that moves away from the sensor, and the positive velocities represent the uplift (blue color) that moves towards the sensor. According to the InSAR-derived results from the Gaofen-3 SAR images, the average subsidence rate ranged from −80 mm/a to 30 mm/a in the vertical direction in the study area. For most metropolitan areas over Beijing, the land subsidence velocity ranged from −15 mm/a to 15 mm/a. It can be seen from Figure 9 that the observed subsidence mainly occurred inside the Chaoyang District and Haidian District (red dashed lines in Figure 9). The primary large-scale subsidence bowl is observed at the northeastern part of Chaoyang District with ~−80 mm/a, where cumulative subsidence was as high as about 40 mm from September 2020 to April 2021, as shown in the time-series results map of the feature points (black star in Figure 9) in Figure 10. There was another subsidence bowl with a relatively lower subsidence velocity at ~−73 mm/a at the northwestern part of Haidian District. The most severe subsidence bowls in Beijing have subsided up to −40 mm from September 2020 to April 2021. As shown in Figure 9, the uplift areas are distributed randomly and caused by some phase noise, and they could not be removed completely from the interferograms due to the limited interferograms for time-series processing.

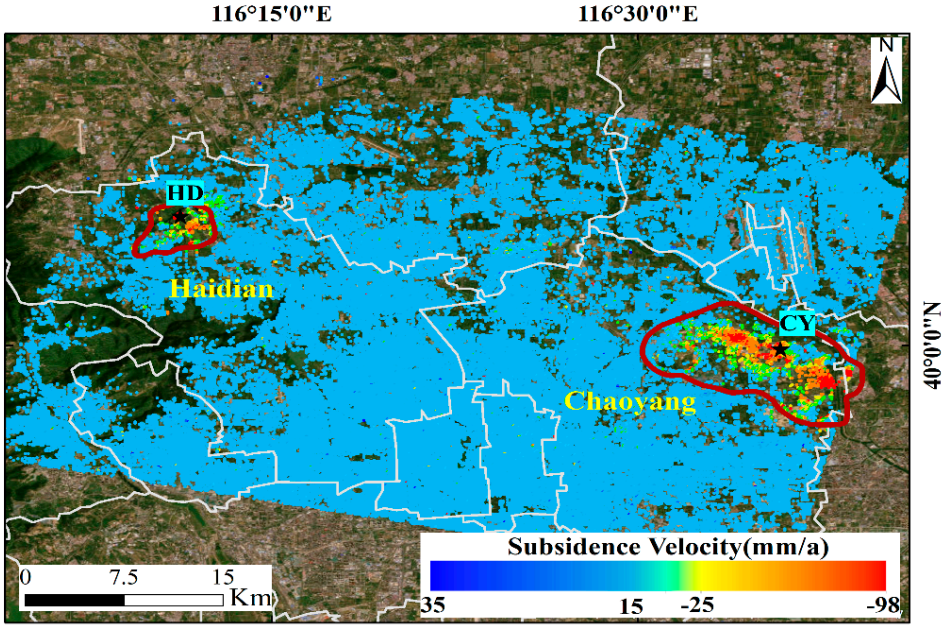

Figure 9. Average subsidence velocity map derived from Gaofen-3 between September 2020 and March 2021, the areas of red dash lines are the main subsidence bowls during the monitoring period.

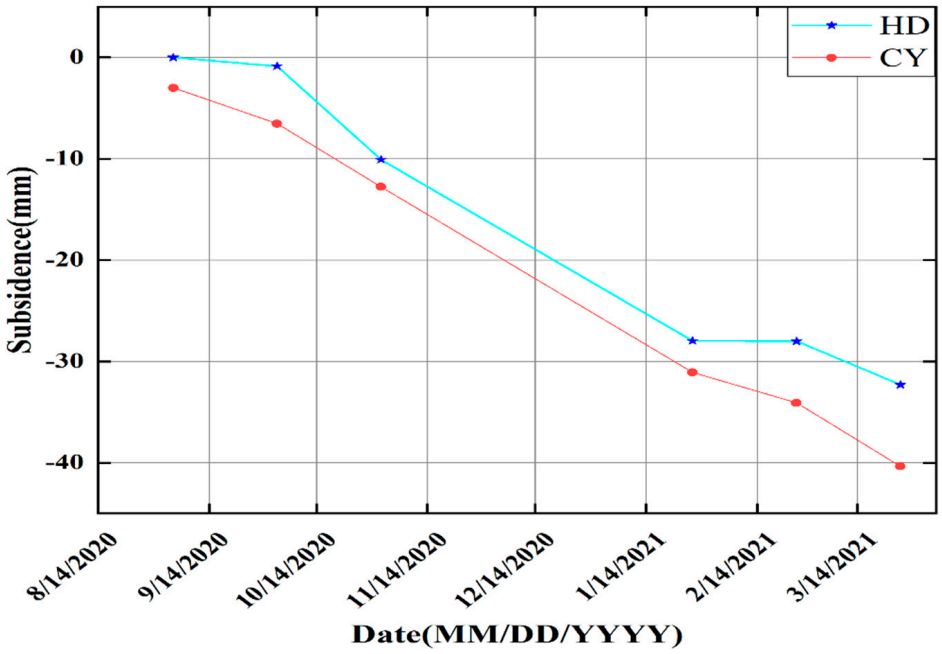

Figure 10. The time series results of feature points (black star) for Gaofen-3 in Figure 9.

5.2. The Comparison with the Results from Sentinel-1 Images

To access the accuracy of InSAR results derived from Gaofen-3 images, both Gaofen-3 and Sentinel-1 SAR images were available over the study area from September 2020 to April 2021. The SBAS-InSAR results derived from the two datasets could be used to cross-validate for the precision of our InSAR results of the Gaofen-3 dataset. As shown in Figures 9 and 11, due to the similar spatial distribution of the subsidence signatures derived from the two independent SAR datasets, the subsidence rates of the Gaofen-3 images agree well with the observations of the Sentinel-1 images. The largest subsidence velocity reached ~−98 mm/a, located at Chaoyang District, but most of the subsidence velocities of the two datasets ranged from ~−80 mm/a to 30 mm/a. To validate the precision of

our InSAR results of the Gaofen-3 images, the subsidence velocity maps were selected to compare the difference between the two independent SAR datasets in vertical directions. Figures 12 and 13 demonstrate the correlation between the Gaofen-3 and Sentinel-1 annual velocity maps, with most of the difference values between the two datasets ranging from −10 to ~10 mm/a, indicating a similar subsidence pattern.

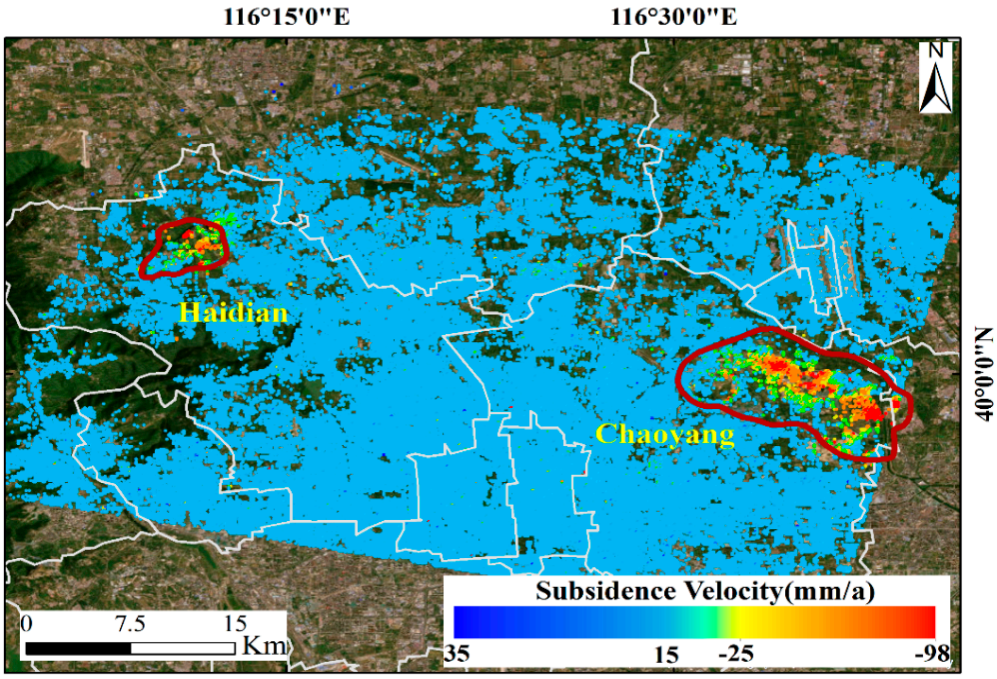

Figure 11. Average subsidence velocity map of Sentinel-1 from August 2020 to April 2021, the areas with red dash lines are the main subsidence bowls during the monitoring period.

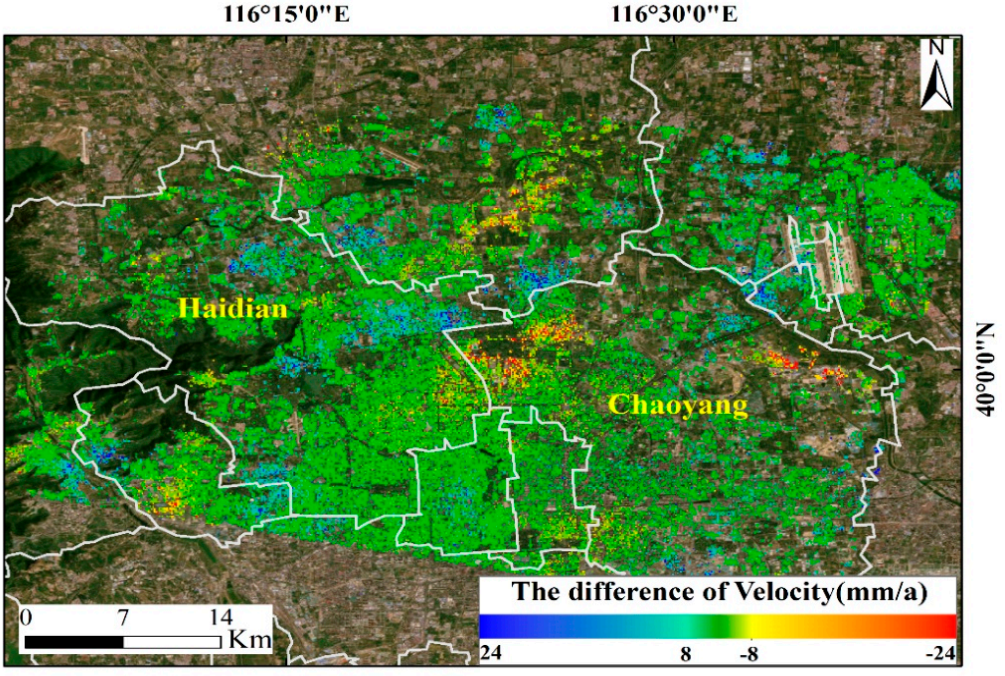

Figure 12. The difference subsidence velocity map between Sentinel-1 (August 2020–April 2021) and Gaofen-3 (September 2020 and March 2021).

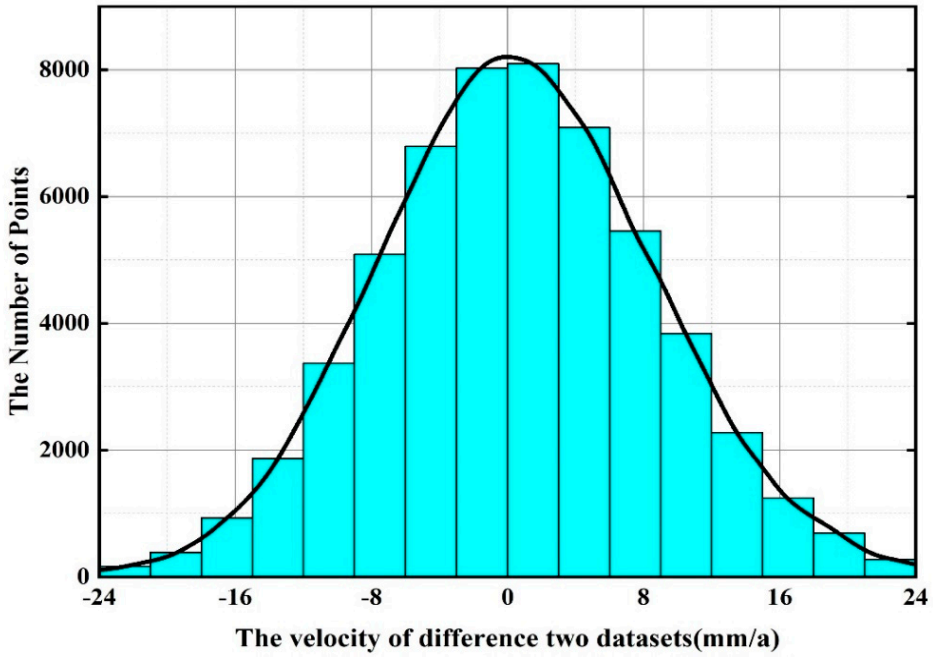

Figure 13. The histograms for the difference in subsidence velocity of the SDFPs measured in the Gaofen-3 and Sentinel-1 SAR datasets.

5.3. The Spatial and Temporal Evolution of Land Subsidence during 2017–2021

Characterizing the variation of Beijing's land subsidence is important not only to warn of and mitigate disasters but also to understand the temporal evolution of land subsidence in Beijing. The Gaofen-3 images could assist in evaluating the spatial and temporal variation of subsidence over Beijing in recent years while comparing them to the measurements derived from Sentinel-1 from 2017 to 2020. Figure 14 highlights the deformation from 2017 to 2020 and from 2020 to 2021 that was calculated with Sentinel-1 and Gaofen-3 SAR data, respectively. Five major subsidence bowls were identified from 2017 to 2021, including three large-scale subsidence bowls located east of the Chaoyang district and northwest of the Haidian district and two relatively small subsidence bowls in the Changping district. The main subsidence bowls show a strong spatial correlation between the period from 2017 to 2020 and from 2020 to 2021, and the subsidence patterns of every subsidence bowl decreased gradually, all of which have experienced significant decelerating in subsidence rates and areas in recent years. The decorrelation may be attributed to the uplift of the groundwater from the South-to-North Water Diversion Project (SNWDP) that has been operating in recent years [21].

The magnitude of the land subsidence inside the three large subsidence bowls decreased gradually during the observation period. We observed that the highest subsidence velocity occurred northeast of the Chaoyang subsidence bowls during both periods, with a maximum value of −122 mm/a from 2017 to 2018, which is much higher than the subsidence velocity from 2020 and 2021, of −80 mm/a. Similar subsidence trends are observed at the Haidian subsidence bowls, and the two small subsidence bowls in Changping district have disappeared since 2019. Even though the extent and scale of all the subsidence decreased gradually, the subsidence bowls inside the district of Chaoyang and Haidian remained subsidence during the observation period, indicating that the land subsidence areas require more attention.

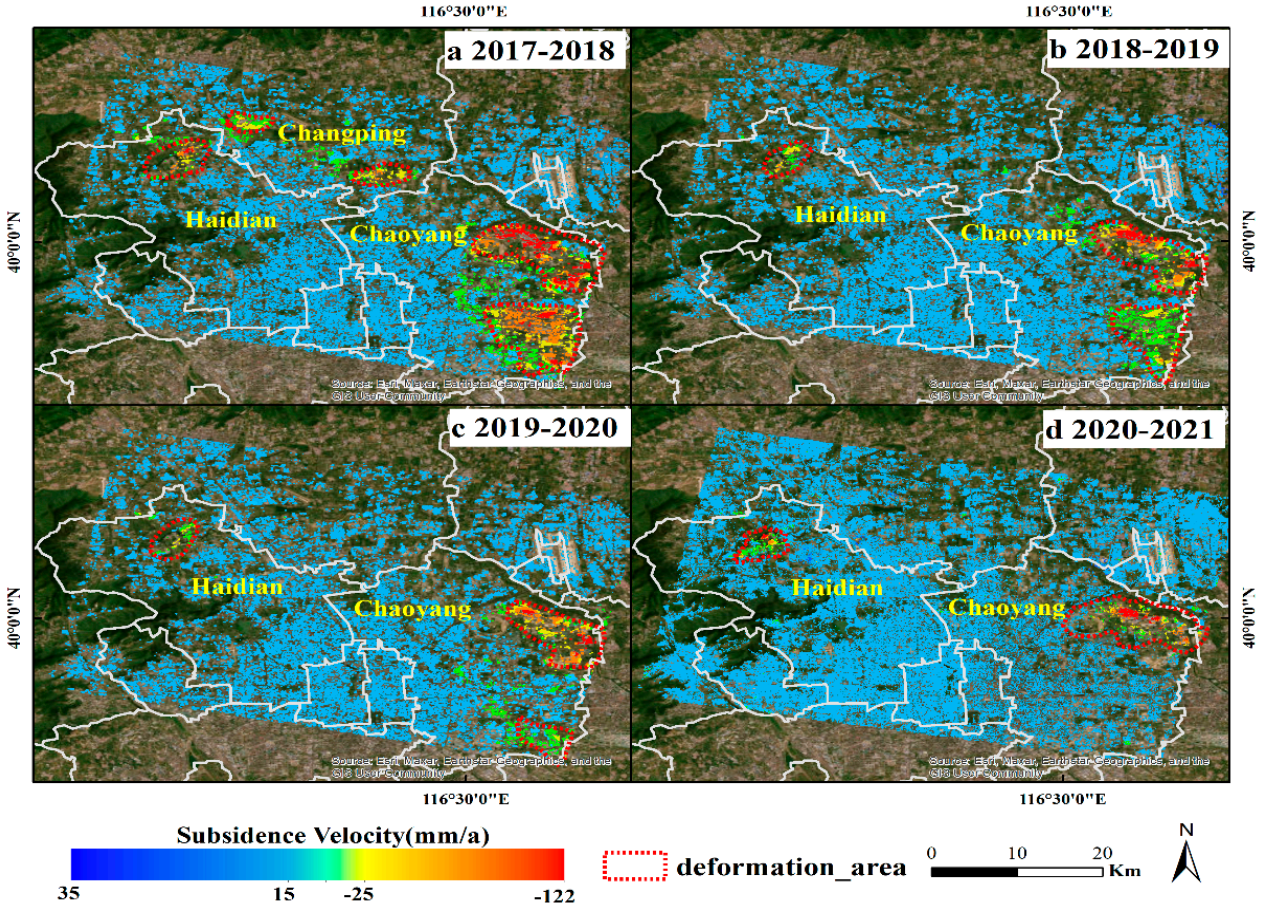

Figure 14. Average subsidence velocity maps derived from Sentinel-1 SAR images and Gaofen-3 SAR images between June 2017 and March 2021: (**a**–**c**) indicate the subsidence velocity map derived from Sentinel-1 images during 2017–2020, (**d**) indicates the subsidence velocity map derived from Gaofen-3 images during 2020–2021.

6. Conclusions

In this study, high-resolution Gaofen-3 SAR images were utilized to measure the land subsidence over the main urban district of Beijing by time series InSAR analysis. Sentinel-1 SAR images were applied to assess the accuracy of subsidence measurements derived from Gaofen-3 SAR images. The subsidence scale and extent are consistent with the detected major subsidence bowls for the two independent SAR datasets, which demonstrates the high accuracy of Gaofen-3 SAR images for measuring the subsidence over the study area. The InSAR results derived from the Gaofen-3 SAR images also revealed the deceleration pattern of the land subsidence over the study area by merging the results derived from the Sentinel-1 SAR images from 2017 to 2020. It is essential for monitoring active subsidence bowls located in the northeastern Chaoyang district.

Our results have demonstrated the Gaofen-3 SAR images' capability of interferometric analysis over the study area, primarily restricted by a long perpendicular baseline and inaccurate orbit information. The long perpendicular baselines decrease the coherence of the interferograms derived from the Gaofen-3 SAR images, while the artifacts with inaccurate orbit information reduce the quality of the interferograms. Refining and reducing the artifacts related to longer perpendicular baselines and inaccurate orbit information from wrapped interferograms will improve the quality of the interferograms of the Gaofen-3 images and assist us in characterizing and revealing the spatial-temporal subsidence patterns over the study areas.

Author Contributions: All the authors participated in editing and reviewing the manuscript. Conceptualization, K.D., T.L. and Y.H.; methodology, Y.H., Z.L. and K.D.; software, Y.H., C.L. and N.W.; data analysis, T.L., Y.H., X.Y. and K.D. Validation, X.S. and X.Z. All authors have read and agreed to the published version of the manuscript.

Funding: This research is funded by the National Key Research and Development Program of China (Grant No. 2021YFB3901403), the National Natural Science Foundation of China (Grant No. 41941019, 41801391, 41871373), the State Key Laboratory of Geohazard Prevention and Geoenvironment Protection Independent Research Project (Grant No. SKLGP2020Z012), Sichuan Province Science Fund for Distinguished Young Scholars (2023NSFSC1909), the fellowship of China Postdoctoral Science Foundation (Grant No. 2020M673322), the Open Fund of Badong National Observation and Research Station of Geohazards (No. BNORSG–202201), and the Open Research Fund Program of MNR Key Laboratory for Geo–Environmental Monitoring of Great Bay Area: 20220006.

Acknowledgments: The authors would like to thank Yuxiao Qin from Northwestern Polytechnical University, Yufen Niu from the Hebei University of Engineering, Feifei Qu from Southern Methodist University, and Wenhao Wu from the Hunan University of Science and Technology for their help in data processing and analyzing the InSAR results. We also like to thank the European Space Agency for providing the Sentinel-1A data and 1 second Copernicus DEM for free.

Conflicts of Interest: The authors declare no conflict of interest.

References

1. Herrera-García, G.; Ezquerro, P.; Tomás, R.; Béjar-Pizarro, M.; López-Vinielles, J.; Rossi, M.; Mateos, R.M.; Carreón-Freyre, D.; Lambert, J.; Teatini, P.; et al. Mapping the Global Threat of Land Subsidence. *Science* **2021**, *371*, 34–36. [CrossRef] [PubMed]
2. Hu, J.; Motagh, M.; Guo, J.; Haghighi, M.H.; Li, T.; Qin, F.; Wu, W. Inferring Subsidence Characteristics in Wuhan (China) through Multitemporal InSAR and Hydrogeological Analysis. *Eng. Geol.* **2022**, *297*, 106530. [CrossRef]
3. Ye, S.; Xue, Y.; Wu, J.; Yan, X.; Yu, J. Progression and Mitigation of Land Subsidence in China. *Hydrogeol. J.* **2016**, *24*, 685–693. [CrossRef]
4. Dai, K.; Li, Z.; Xu, Q.; Bürgmann, R.; Milledge, D.G.; Tomas, R.; Fan, X.; Zhao, C.; Liu, X.; Peng, J.; et al. Entering the Era of Earth Observation-Based Landslide Warning Systems: A Novel and Exciting Framework. *IEEE Geosci. Remote Sens. Mag.* **2020**, *8*, 136–153. [CrossRef]
5. Wright, T.J.; Parsons, B.E.; Lu, Z. Toward Mapping Surface Deformation in Three Dimensions Using InSAR. *Geophys. Res. Lett.* **2004**, *31*. [CrossRef]
6. Ferretti, A.; Colombo, D.; Fumagalli, A.; Novali, F.; Rucci, A. InSAR Data for Monitoring Land Subsidence: Time to Think Big. *Proc. Int. Assoc. Hydrol. Sci.* **2015**, *372*, 331–334. [CrossRef]
7. Hu, X.; Lu, Z.; Wang, T. Characterization of Hydrogeological Properties in Salt Lake Valley, Utah, Using InSAR. *J. Geophys. Res. Earth Surf.* **2018**, *123*, 1257–1271. [CrossRef]
8. Zhao, C.; Liu, C.; Zhang, Q.; Lu, Z.; Yang, C. Deformation of Linfen-Yuncheng Basin (China) and Its Mechanisms Revealed by ΠI-RATE InSAR Technique. *Remote Sens. Environ.* **2018**, *218*, 221–230. [CrossRef]
9. Bekaert, D.P.; Handwerger, A.L.; Agram, P.; Kirschbaum, D.B. InSAR-Based Detection Method for Mapping and Monitoring Slow-Moving Landslides in Remote Regions with Steep and Mountainous Terrain: An Application to Nepal. *Remote Sens. Environ.* **2020**, *249*, 111983. [CrossRef]
10. Dai, K.; Deng, J.; Xu, Q.; Li, Z.; Shi, X.; Hancock, C.; Wen, N.; Zhang, L.; Zhuo, G. Interpretation and Sensitivity Analysis of the InSAR Line of Sight Displacements in Landslide Measurements. *GIScience Remote Sens.* **2022**, *59*, 1226–1242. [CrossRef]
11. Lu, Z.; Dzurisin, D. InSAR Imaging of Aleutian Volcanoes. In *InSAR Imaging of Aleutian Volcanoes*; Springer: Berlin/Heidelberg, Germany, 2014; pp. 87–345.
12. Yang, Z.; Li, Z.; Zhu, J.; Wang, Y.; Wu, L. Use of SAR/InSAR in Mining Deformation Monitoring, Parameter Inversion, and Forward Predictions: A Review. *IEEE Geosci. Remote Sens. Mag.* **2020**, *8*, 71–90. [CrossRef]
13. Gourmelen, N.; Kim, S.; Shepherd, A.; Park, J.; Sundal, A.; Björnsson, H.; Pálsson, F. Ice Velocity Determined Using Conventional and Multiple-Aperture InSAR. *Earth Planet. Sci. Lett.* **2011**, *307*, 156–160. [CrossRef]
14. Qiu, X. A Novel Proposal of Gaofen-3 Satellite Constellation for Multi-Applications. *Int. Arch. Photogramm. Remote Sens. Spatial Inf. Sci.* **2017**, *XLII-2/W7*, 635–639. [CrossRef]
15. Ren, L.; Yang, J.; Mouche, A.; Wang, H.; Wang, J.; Zheng, G.; Zhang, H. Preliminary Analysis of Chinese GF-3 SAR Quad-Polarization Measurements to Extract Winds in Each Polarization. *Remote Sens.* **2017**, *9*, 1215. [CrossRef]
16. Yang, J.; Yuan, X.; Han, B.; Zhao, L.; Sun, J.; Shang, M.; Wang, X.; Ding, C. Phase Imbalance Analysis of GF-3 Along-Track InSAR Data for Ocean Current Measurement. *Remote Sens.* **2021**, *13*, 269. [CrossRef]
17. Zheng, Y.; Chen, Z.; Zhang, G. Application and Evaluation of the Gaofen-3 Satellite on a Terrain Survey with InSAR Technology. *Appl. Sci.* **2020**, *10*, 806. [CrossRef]

18. Wang, J.; Yu, W.; Deng, Y.; Wang, R.; Wang, Y.; Zhang, H.; Zheng, M. Demonstration of Time-Series InSAR Processing in Beijing Using a Small Stack of Gaofen-3 Differential Interferograms. *J. Sens.* **2019**, *2019*, 4204580. [CrossRef]
19. Zhang, Y.; Wu, H.; Kang, Y. Ground Subsidence over Beijing-Tianjin-Hebei Region during Three Periods of 1992 to 2014 Monitored by Interferometric SAR. *Acta Geod. Cartogr. Sin.* **2016**, *45*, 1050.
20. Chen, B.; Gong, H.; Li, X.; Lei, K.; Zhu, L.; Gao, M.; Zhou, C. Characterization and Causes of Land Subsidence in Beijing, China. *Int. J. Remote Sens.* **2017**, *38*, 808–826. [CrossRef]
21. Guo, L.; Gong, H.; Li, J.; Zhu, L.; Xue, A.; Liao, L.; Sun, Y.; Li, Y.; Zhang, Z.; Hu, L.; et al. Understanding Uneven Land Subsidence in Beijing, China, Using a Novel Combination of Geophysical Prospecting and InSAR. *Geophys. Res. Lett.* **2020**, *47*, e2020GL088676. [CrossRef]
22. Zhu, L.; Gong, H.; Chen, Y.; Wang, S.; Ke, Y.; Guo, G.; Li, X.; Chen, B.; Wang, H.; Teatini, P. Effects of Water Diversion Project on Groundwater System and Land Subsidence in Beijing, China. *Eng. Geol.* **2020**, *276*, 105763. [CrossRef]
23. Du, Z.; Ge, L.; Ng, A.H.-M.; Lian, X.; Zhu, Q.; Horgan, F.G.; Zhang, Q. Analysis of the Impact of the South-to-North Water Diversion Project on Water Balance and Land Subsidence in Beijing, China between 2007 and 2020. *J. Hydrol.* **2021**, *603*, 126990. [CrossRef]
24. Liang, F.; Sun, J.; Shen, Z.; Xu, X. Accumulated Crustal Deformation and Its Characteristics in Beijing and Surrounding Regions in 2007–2010 from L-Band InSAR. *Earthquake* **2013**, *33*, 43–54.
25. Ng, A.H.-M.; Ge, L.; Li, X.; Zhang, K. Monitoring Ground Deformation in Beijing, China with Persistent Scatterer SAR Interferometry. *J. Geod.* **2012**, *86*, 375–392. [CrossRef]
26. Chen, B.; Gong, H.; Chen, Y.; Li, X.; Zhou, C.; Lei, K.; Zhu, L.; Duan, L.; Zhao, X. Land Subsidence and Its Relation with Groundwater Aquifers in Beijing Plain of China. *Sci. Total Environ.* **2020**, *735*, 139111. [CrossRef]
27. Zhang, S.; Zhang, Y.; Yu, J.; Fan, Q.; Si, J.; Zhu, W.; Song, M. Interpretation of the Spatiotemporal Evolution Characteristics of Land Deformation in Beijing during 2003–2020 Using Sentinel, ENVISAT, and Landsat Data. *Remote Sens.* **2022**, *14*, 2242. [CrossRef]
28. Zhou, C.; Gong, H.; Chen, B.; Li, X.; Li, J.; Wang, X.; Gao, M.; Si, Y.; Guo, L.; Shi, M.; et al. Quantifying the Contribution of Multiple Factors to Land Subsidence in the Beijing Plain, China with Machine Learning Technology. *Geomorphology* **2019**, *335*, 48–61. [CrossRef]
29. Bai, Z.; Wang, Y.; Balz, T. Beijing Land Subsidence Revealed Using PS-InSAR with Long Time Series TerraSAR-X SAR Data. *Remote Sens.* **2022**, *14*, 2529. [CrossRef]
30. Zhou, Z.; Yao, X.; Ren, K.; Liu, H. Formation Mechanism of Ground Fissure at Beijing Capital International Airport Revealed by High-Resolution InSAR and Numerical Modelling. *Eng. Geol.* **2022**, *306*, 106775. [CrossRef]
31. Du, Z.; Ge, L.; Ng, A.H.-M.; Xiaojing, L.; Li, L. Mapping Land Subsidence over the Eastern Beijing City Using Satellite Radar Interferometry. *Int. J. Digit. Earth* **2018**, *11*, 504–519. [CrossRef]
32. Liu, B.; Li, M.; Zhang, L.; Ge, D. Monitoring Beijing-Tianjin Region Land Subsidence Using ALOS-2 Scansar Images. In Proceedings of the 2021 IEEE International Geoscience and Remote Sensing Symposium IGARSS, Brussels, Belgium, 11–16 July 2021; IEEE: Piscataway, NJ, USA, 2021; pp. 5338–5341.
33. Ning, J.; Wang, R.; Wang, J.; Zhang, B.; Zhao, S. Ionospheric Correction of ALOS-2 Full-Aperture ScanSAR Interferometric Data for Surface Deformation Measurement in Beijing. *J. Eng.* **2019**, *2019*, 5685–5688. [CrossRef]
34. Hu, L.; Dai, K.; Xing, C.; Li, Z.; Tomás, R.; Clark, B.; Shi, X.; Chen, M.; Zhang, R.; Qiu, Q.; et al. Land Subsidence in Beijing and Its Relationship with Geological Faults Revealed by Sentinel-1 InSAR Observations. *Int. J. Appl. Earth Obs. Geoinf.* **2019**, *82*, 101886. [CrossRef]
35. Chen, B.; Gong, H.; Lei, K.; Li, J.; Zhou, C.; Gao, M.; Guan, H.; Lv, W. Land Subsidence Lagging Quantification in the Main Exploration Aquifer Layers in Beijing Plain, China. *Int. J. Appl. Earth Obs. Geoinf.* **2019**, *75*, 54–67. [CrossRef]
36. Zhang, Y.; Gong, H.; Gu, Z.; Wang, R.; Li, X.; Zhao, W. Characterization of Land Subsidence Induced by Groundwater Withdrawals in the Plain of Beijing City, China. *Hydrogeol. J.* **2014**, *22*, 397–409. [CrossRef]
37. Hassen, R. *Radar Interferometry*; Kluwer Academic Publishers: Alphen am Rhine, The Netherlands, 2001.
38. Ferretti, A. *Satellite InSAR Data: Reservoir Monitoring from Space*; EAGE Publications: Bunnik, The Netherlands, 2014.
39. Foroughnia, F.; Nemati, S.; Maghsoudi, Y.; Perissin, D. An Iterative PS-InSAR Method for the Analysis of Large Spatio-Temporal Baseline Data Stacks for Land Subsidence Estimation. *Int. J. Appl. Earth Obs. Geoinf.* **2019**, *74*, 248–258. [CrossRef]
40. Li, J.; Xin, J. Research on Flat Earth Removal Techniques of INSAR. *Adv. Mater. Res.* **2012**, *433*, 7487–7492. [CrossRef]
41. Berardino, P.; Fornaro, G.; Lanari, R.; Sansosti, E. A New Algorithm for Surface Deformation Monitoring Based on Small Baseline Differential SAR Interferograms. *IEEE Trans. Geosci. Remote Sens.* **2002**, *40*, 2375–2383. [CrossRef]
42. Qu, F.; Lu, Z.; Zhang, Q.; Bawden, G.W.; Kim, J.-W.; Zhao, C.; Qu, W. Mapping Ground Deformation over Houston–Galveston, Texas Using Multi-Temporal InSAR. *Remote Sens. Environ.* **2015**, *169*, 290–306. [CrossRef]
43. Hooper, A.; Zebker, H.; Segall, P.; Kampes, B. A New Method for Measuring Deformation on Volcanoes and Other Natural Terrains Using InSAR Persistent Scatterers. *Geophys. Res. Lett.* **2004**, *31*. [CrossRef]
44. Galve, J.P.; Pérez-Peña, J.V.; Azañón, J.M.; Closson, D.; Caló, F.; Reyes-Carmona, C.; Jabaloy, A.; Ruano, P.; Mateos, R.M.; Notti, D.; et al. Evaluation of the SBAS InSAR Service of the European Space Agency's Geohazard Exploitation Platform (GEP). *Remote Sens.* **2017**, *9*, 1291. [CrossRef]
45. Ferretti, A.; Prati, C.; Rocca, F. Permanent Scatterers in SAR Interferometry. *IEEE Trans. Geosci. Remote Sens.* **2001**, *39*, 8–20. [CrossRef]

46. Hooper, A.; Segall, P.; Zebker, H. Persistent Scatterer InSAR for Crustal Deformation Analysis, with Application to Volcán Alcedo, Galápagos. *J. Geophys. Res.* **2007**, *112*, 19.
47. Qu, F.; Zhang, Q.; Niu, Y.; Lu, Z.; Wang, S.; Zhao, C.; Zhu, W.; Qu, W.; Yang, C. Mapping the Recent Vertical Crustal Deformation of the Weihe Basin (China) Using Sentinel-1 and ALOS-2 ScanSAR Imagery. *Remote Sens.* **2022**, *14*, 3182. [CrossRef]
48. Qu, F.; Zhang, Q.; Lu, Z.; Zhao, C.; Yang, C.; Zhang, J. Land Subsidence and Ground Fissures in Xi'an, China 2005–2012 Revealed by Multi-Band InSAR Time-Series Analysis. *Remote Sens. Environ.* **2014**, *155*, 366–376. [CrossRef]
49. Hooper, A. A Multi-Temporal InSAR Method Incorporating Both Persistent Scatterer and Small Baseline Approaches. *Geophys. Res. Lett.* **2008**, *35*. [CrossRef]
50. Hooper, A.; Zebker, H.A. Phase Unwrapping in Three Dimensions with Application to InSAR Time Series. *JOSA A* **2007**, *24*, 2737–2747. [CrossRef]
51. Bueso-Bello, J.-L.; Martone, M.; Prats-Iraola, P.; Bräutigam, B. First Characterization and Performance Evaluation of Bistatic TanDEM-X Experimental Products. *IEEE J. Sel. Top. Appl. Earth Obs. Remote Sens.* **2015**, *9*, 1058–1071. [CrossRef]